Chapter 3

Tools for mid-IR analysis of AGB dust

Mid-IR is the ideal spectral range to study circumstellar dust. The presence of broad features in the opacity of grain commonly formed in the extended atmosphere of giant stars, in principle allows a precise identification of the mineralogical species by analyzing the 10 μm spectra. The temperature gradients in circumstellar envelopes, with dust in equilibrium with the environmental radiation field, are such that the bulk of the grain thermal radiation is emitted in the 10 μm region. Since the optical thickness of many circumstellar envelopes, especially around AGB stars, is high enough to make them completely opaque at visible wavelengths, mid-IR is the only accessible spectral window for probing the central region of these systems.

For these basic reasons the IRAS database has been widely used for the development of diagnostic tools able to probe the chemical and physical status of circumstellar envelopes from their infrared emission. This approach, however, is limited by the low spatial and spectral resolution of IRAS data, and the impossibility to make repeated observations of variable sources. Even though a limited number of sources have been subjected to new observations with the european satellite ISO, these issues have not been completely resolved, due to the short duration of the mission, serious calibration problems and the still inadequate spatial resolution. These limitations confirm the need for ground based high resolution facilities, monitoring the status of AGB circumstellar envelopes in the mid-IR over long periods of time.

This chapter is devoted to the presentation of a new set of tools for the analysis of ground-based mid-IR photometry of AGB circumstellar en-

velopes. The results of this analysis have been presented in the paper Marengo et al. (1999), and have been obtained in collaboration with Maurizio Busso at the Astronomical Observatory of Torino (Italy), Giovanni Silvestro at the "Dipartimento di Fisica Generale", University of Torino (Italy), Paolo Persi at the "Istituto di Astrofisica Spaziale" of the Italian National Research Council (C.N.R. Roma) and Pierre-Olivier Lagage at the "Service d'Astrophysique", CEA Saclay (France).

A sample of AGB sources with known mass loss rates, introduced in section 3.3.2, is used for calibration purposes, and to explore the correlations between the infrared emissions and mass loss of the selected sources. The calibration is then confirmed by radiative transfer modeling of spherically symmetric AGB systems, as it is described in detail in section 3.2.

3.1 Asymptotic Giant Branch Stars

It has already been pointed out that AGB stars are collectively the main source of *stardust* in the Galaxy. Providing a large fraction of the carbon from which the solar system (and ultimately, the biological life) is made, AGB stars play an important role in the chemical evolution of the ISM. AGB stars contribute a large fraction of the infrared luminosity of galaxies, and are thus one of the main components of stellar population synthesis models aiming to reproduce galactic spectra in the IR. Finally, stars on the AGB represent an almost ideal laboratory for nuclear physics and stellar evolution theories, since convection reaching their internal burning shells drags to the surface recently synthesized nuclei, exposing them to direct observation.

In all these processes, the less known ingredient is probably the strong mass loss that characterize the AGB phase, which is enhanced by the presence of dust, and powered by even less known processes of dust nucleation in the stellar extended atmosphere.

The analysis of the AGB circumstellar envelopes from the point of view of mid-IR astronomy, to which a large part of this thesis is devoted, should thus be seen as an effort to open a new channel for researching one of the key factors in the evolution of the Galaxy, and the physics involved.

In this section the relevant facts about AGB stars are given. For a more general discussion of AGB evolution and nucleosynthesis the reader is referred to Busso et al. (1999) and Wallerstein & Knapp (1998), where the various classes of carbon stars are discussed in length.

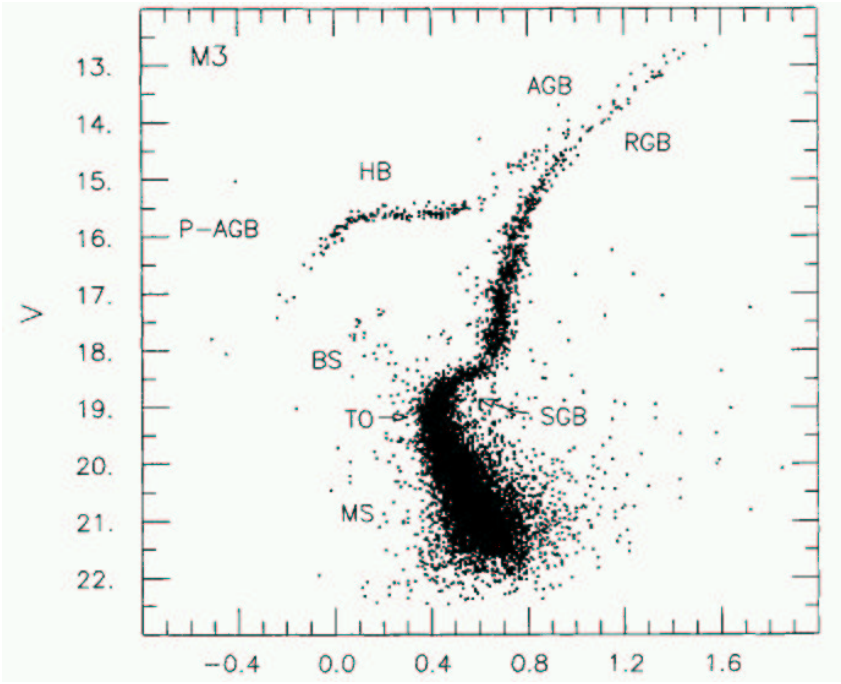

FIG. 3.1.— The Asymptotic Giant Branch in the Hertzsprung-Russel diagram of the globular cluster M3. Adapted from Renzini & Fusi Pecci (1988)

3.1.1 Evolution of low and intermediate mass stars

The Asymptotic Giant Branch phase represents the second ascent of intermediate and low mass stars in the red giant region of the Hertzsprung-Russel diagram (see figure 3.1). Stars with main sequence mass below 6-8 $M_{\odot}$, after the exhaustion of H core burning, rise the Hayashi tracks in the HR diagram, gradually reaching higher luminosities and lower effective temperatures. This is done with the expansion of their convective envelope by several orders of magnitude, ending with a stellar radius of the order of a few A.U. Sustained by nuclear burning of H in a shell, around an inert He core, these stars populate the region of the HR diagram known as Red Giant Branch (RGB).

Towards the end of the RGB, the convective envelopes of giants reach the internal layers of these stars, processed by previous nucleosynthesis. As a result, the surface abundance of ^{14}N is doubled, ^{12}C is reduced by 30% and Li and Be are diluted by several orders of magnitude (Iben & Renzini, 1983). This process is called *first dredge-up*.

The RGB phase ends with the ignition of the He shell, which replaces the H shell as main energy source; the star contracts, increase its effective temperature, and enters in the *Horizontal Branch* (HB). Low mass stars, having $M_i \lesssim 1.8$–2.2 $M_\odot$ (Chiosi et al., 1992), which develop a degenerate He core during the RGB, experience the so-called He-flash, in which the degeneration is removed. Intermediate mass stars, on the contrary, start core He burning in normal conditions, in the *blue band* region of the HR diagram, which ends with a rapid contraction of the H convective envelope (*blue loop*).

In both cases, the HB phase ends with the creation of an inert C-O core, around which a burning He shell is active. Stars with $M_i \gtrsim 6$–8 $M_\odot$will instead ignite C burning in the core, starting a path which will ultimately lead to their explosion as Type II supernovæ.

The Sun is a low mass stars, and will thus become a Red Giant after leaving the main sequence. This moment in the solar evolution will mark the destruction of the inner solar system, among which the planet Earth.

3.1.2 The Early-AGB phase

The AGB starts with the exhaustion of He core burning, and is divided in two phases: Early-AGB (E-AGB) in which the He burning shell provides all the energy necessary to sustain the stellar structure, and the thermal pulsing AGB (TP-AGB) which is characterized by the alternate ignition of two concentric He and H shells.

The E-AGB is accompanied by a progressive contraction of the core, which become highly degenerate ($\rho_c \sim 10^6$ g cm^{-3}) and isothermal, due to the high conductivity of the Fermi pressure of free degenerate electrons. The high efficiency of neutrino cooling processes (Urca) helps to mantain a low core temperature ($Tc \sim 2 \cdot 10^8$K), well below the C ignition temperature.

At the end of the E-AGB, intermediate mass stars experience a *second dredge-up*, in which elements processed by the CNO cycle are taken to the surface, which increases in abundance of ^{4}He and ^{14}N, at the expense of ^{12}C and ^{16}O.

The E-AGB phase ends when the He shell is extinguished, and the H burning starts again in a new external shell. This typically happens when the mass of the H depleted core reaches the critical value of ~ 0.5–0.6 $M_\odot$ (Becker & Iben, 1979).

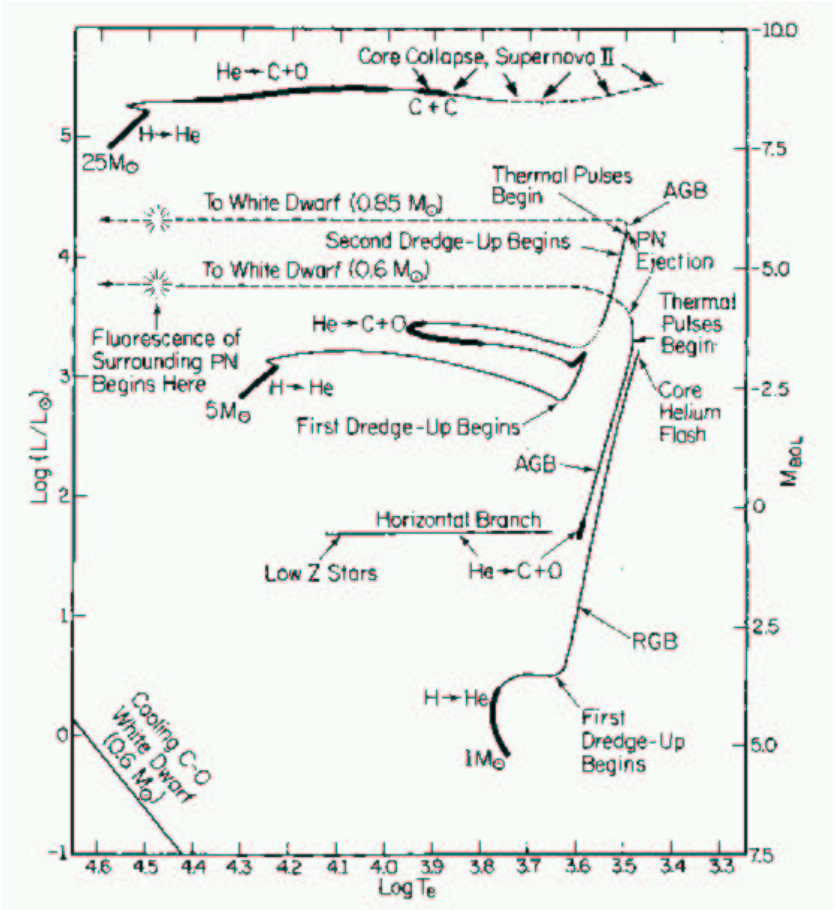

FIG. 3.2.— Tracks on the HR diagram of theoretical model stars of low (1 $M_\odot$), intermediate (5 $M_\odot$) and high (25 $M_\odot$) mass. From Iben (1991)

3.1.3 The TP-AGB phase and the third dredge-up

The second part of the AGB is characterized by thermal instabilities called *thermal pulses*. A thermal pulse occurs when the He shell, which continously increases in mass due to the burning of the external H shell, is momentarily ingnited and expands. This expansion is reversed when the temperature drops below the minimum necessary for He burning; the He shell is extinguished again and the H burning restarts. The duration of the He shell activity is very short ($\sim 10^2$ yr), and the cycle is repeated every 10^3-10^4 yr. The lenght of the interpulse period is a function of the C-O core mass, and can thus be quite different between low and intermediate mass stars:

$$\tau_{ip} \sim 2 \cdot 10^5 \,\mathrm{yr} \left(\frac{0.6 \mathrm{M}_\odot}{M_{C-O}} \right)^{10} \tag{3.1}$$

In fact, since the core mass is increased at each thermal pulse with the C and O produced during the He burning, the interpulse period becomes shorter at the very end of the TP-AGB, when a rapid sequence of thermal pulses is experienced. During a thermal pulse, the luminosity produced by the star is largely increased; in the long interpulse phase, however, the total luminosity tends asymptotically to a value controlled by the H depleted core mass (Paczynski, 1970; Uus, 1970):

$$L_{max} = 5.925 \cdot 10^4 \left(\frac{M_H}{1 \,\mathrm{M}_\odot} - 0.495 \right) \mathrm{L}_\odot \tag{3.2}$$

Immediately after a thermal pulse, the base of the convective envelope penetrates (in mass) in the regions that contains freshly produced elements, causing a new dredge-up (*third dredge-up*). The third dredge-up is responsible for the increase of surface abundance of C, in stars which are initially O-rich M giants. Neutron rich elements produced during the thermal pulses by repeated exposures with intense neutron fluxes (*s-elements*) are also dragged to the surface. Since many s-elements are short lived radioactive nuclei (as in the case of Tc), their detection in a stellar spectra is the best evidence that the object is presently in the TP-AGB phase.

Recently updated stellar models (Straniero et al., 1995, 1997) found that, for solar metallicity, stars above the 1.5–2 $\mathrm{M}_\odot$ can undergo a sufficient number of third dredge-up episodes to drive an increase of the C/O ratio above unity. When this happens, a *carbon star* is born. On the other end, AGB stars with $M_i \gtrsim$ 5-6 $\mathrm{M}_\odot$ experience partial H burning at the base of the convective envelope, or Hot Bottom Burning, HBB, (see e.g. Sugimoto, 1971; Renzini & Voli, 1981; Blöcker & Schönberner, 1991; Sackmann & Boothroyd, 1992; Vassiliadis & Wood, 1993; Frost et al., 1998). This consumes the newly produced C, preventing the star from becoming C-rich, and enriches the stellar surface with Li (however, see Frost et al., 1998, for an alternative evolutionary path). As a result, C stars can probably be formed at the end of the AGB evolution, only for a quite narrow mass range (2–4 $\mathrm{M}_\odot$), with more massive stars remaining as Li-rich objects, generally of class S if the abundance of s-elements is high enough to be observable (Smith & Lambert, 1989).

During the TP-AGB phase, the mass loss already present in the RGB and E-AGB is enhanced, due to the formation of dust in the stellar extended

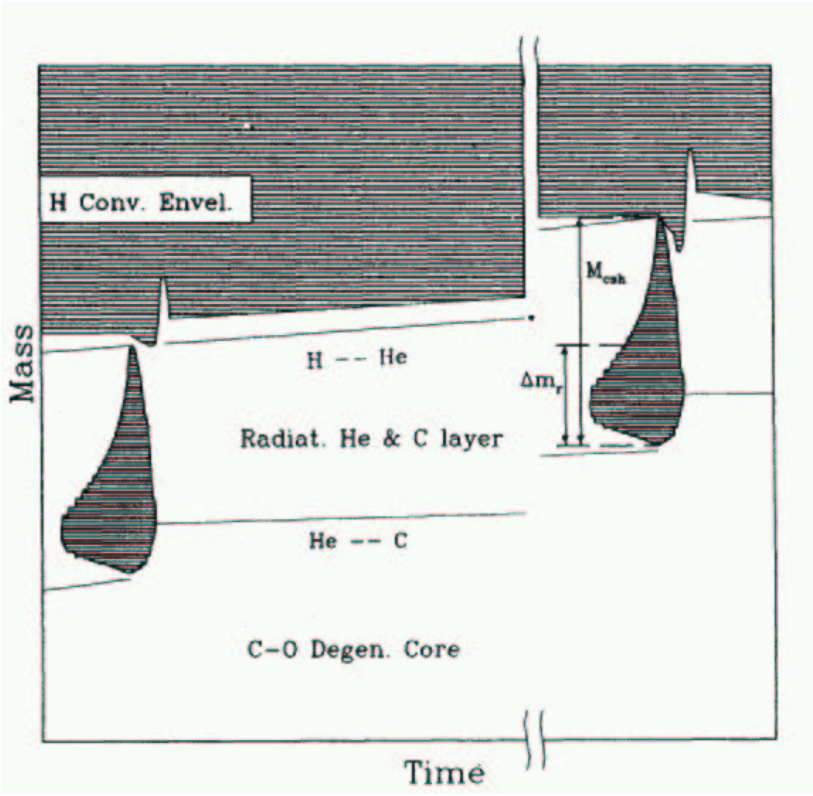

FIG. 3.3.— Simplified sketch of the structure of the stellar layers outside the degenerate C-O core, during two successive thermal pulses. Shaded regions are convective, and dredge-up from the convective envelope is shown after each pulse. From Busso et al. (1995)

atmosphere, powering strong stellar winds at the expenses of the stellar convective envelope. The end of the AGB comes when the star is totally depleted of its convective envelope, and the hot degenerate core is exposed. The star then becomes a post-AGB object, on its way to its final state of white dwarf.

3.1.4 The AGB mass loss

Mass loss is a common characteristic of giant stars; what is peculiar of the AGB phase, however, is the *magnitude* of the mass loss rate, which in just a few final stellar pulses transforms an intermediate mass star into a 0.5–0.6 $M_\odot$ white dwarf. Where does all the convective envelope mass go? It

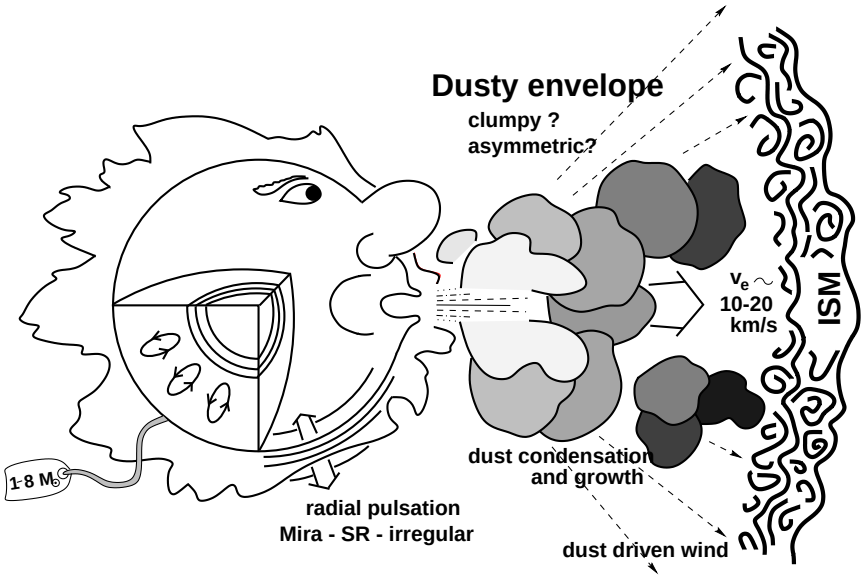

FIG. 3.4.— The main components of an AGB system: the central TP-AGB star producing a strong *dust driven* stellar wind, and the dusty circumstellar envelope merging with the ISM. From Marengo et al. (2000b)

ends up dispersed in the circumstellar environment, with the creation of a circumstellar envelope of gas and dust which will ultimately merge with the ISM (see section 1.2.3).

A complete theory able to explain the required mass loss rates (up to 10^{-4} $\mathrm{M}_\odot$ yr^{-1}) is presently unavailable. The RGB mass loss can be easily explained by using a *Reimers wind* formula, in which the mass loss rates is a function of the stellar luminosity, radius and mass (Reimers, 1975):

$$\dot{M} \sim 4 \cdot 10^{-13} \, \mathrm{M}_\odot \, \mathrm{yr}^{-1} \, \eta \left(\frac{L_*}{1 \, \mathrm{L}_\odot} \right) \left(\frac{R_*}{1 \, \mathrm{R}_\odot} \right) \left(\frac{1 \, \mathrm{M}_\odot}{M_*} \right) \tag{3.3}$$

where η is a fudge factor between 1/3 and 3. The mass loss predicted by the Reimers formula is largely insufficient to describe the AGB mass loss rates. Larger values of $\dot{M}$ can be obtained applying a semi-empirical formula derived by Salpeter (1974), in which is assumed that the total momentum of the expanding envelope is given by the radiation pressure acting on the circumstellar dust grains:

$$\dot{M} \sim 2 \cdot 10^{-8} \, \mathrm{M}_\odot \, \mathrm{yr}^{-1} \, \tau_V \left(\frac{L_*}{1 \, \mathrm{L}_\odot} \right) \left(\frac{1 \, \mathrm{km \ s}^{-1}}{v_e} \right) \tag{3.4}$$

where τ_V is the total optical depth of the envelope (mainly given by the dust), v_e is the envelope expansion speed, and L_* the stellar luminosity.

Many modifications of these two mass loss formulas, specifically written for the AGB phase, have been proposed; a good review is given in Habing (1996). As in the case of Salpeter's wind, the main idea is that the AGB wind is powered by the stellar radiation acting on the dust grains, which then transfers the momentum to the gaseous component of the envelope (*dust driven winds*). The only difficulty with this idea is that it requires a separate "engine" to accumulate enough material to start up the process at a suitable distance from the star, where the temperature is low enough to allow dust grain condensation. To solve this problem, the effects of radial pulsations related to the long period variability of many AGB stars, are invoked: this scenario is discussed in detail in chapter 4, where the correlation between mass loss and stellar variability via radiative transfer modeling of the observed IR spectra is analyzed.

In any case, the AGB mass loss is strong enough to enshroud low and intermediate mass stars with optically thick circumstellar envelopes made at the expense of the stellar convective envelopes, thus preventing such stars to grow their core mass above the limits that would otherwise lead to a Type II supernova event, as is the case for the fast evolving massive stars. The death of an AGB star (and thus of our Sun) is a quiet one, and happens hidden inside dusty cocoon: "*old soldiers never die, they simply fade away*" (from Habing, 1990).

3.1.5 The post-AGB phase, and beyond

The post-AGB is a brief transition phase in which the star leaves the tip of the AGB, crossing the HR diagram at constant luminosity towards the white dwarf region. Most of the post-AGB objects are heavily obscured by their optically thick dust envelopes, that dissipate only when the effective temperature of the star becomes high enough to trigger the formation of a fast pressure-driven *superwind*, which blows away the AGB envelope. When this happens, the energetic radiation from the hot central object, now a white dwarf, ionizes and excites the circumstellar molecular gas, creating a Planetary Nebula.

The creation of a planetary nebula is a complex phenomenon which involves time dependent hydrodynamics and radiative transfer. A simplified model was created by Kwok et al. (1978), by assuming a process of *interacting stellar winds* (the slow moving AGB wind, responsible for the dusty circumstellar envelopes, and the fast post-AGB superwind). This model

shows that, after the onset of the superwind, the shock front that propagates through the fossil AGB envelope completely changes its structure, making worthless any attempt to reconstruct the mass loss history of the AGB precursor from the density profile of the PN dusty halo. High resolution imaging of the AGB and post-AGB phases, which are before the start of the superwind, are thus necessary to probe the history of mass loss by observing the circumstellar envelope.

The interacting stellar winds model, however, cannot deal with the complex morphology observed in PN. As shown in the gorgeous gallery collected by the Hubble Space Telescope, many, if not all, of the planetary nebulæ possess various degree of asymmetry. HST and Mid-IR imaging surveys have revealed that these asymmetric structures are already present in the post-AGB phase (Ueta et al., 2000; Meixner et al., 1999); it is not clear, however, when the departure from sphericity starts, since AGB stars are presumed to be spherically symmetric systems.

3.2 Modeling the mid-IR spectra of AGB envelopes

The main tool to study the infrared spectral energy distribution of AGB circumstellar envelopes is represented by radiative transfer modeling. This is a common practice, that has been applied to derive the physical parameters of AGB dust shells by many authors (Rowan-Robinson, 1980; Griffin., 1990; Justtanont & Tielens, 1992; Hashimoto, 1995; Ivezić & Elitzur, 1995; Marengo et al., 1997, and many others). All these works have been using a model based on the fundamental equations described in section 2.1, in the approximation of spherical symmetry, and envelope radial density structure determined by the hypothesis of steady mass loss ($n_d \propto y^{-2}$) or static dust driven wind (Ivezić & Elitzur, 1995). More recently, sophisticated models taking into account time dependent hydrodynamics (Steffen et al., 1998), dust formation and dynamic coupling between the base of the circumstellar envelope and a fully self-consistent pulsating AGB stellar atmosphere (Winters et al., 1994; Windsteig et al., 1997; Höfner & Dorfi, 1997) have been developed. Two dimensional models able to deal with complex envelope geometries (Lopez et al., 1995) have also been applied to specific sources, whose images were showing actual departures from spherical symmetry.

Due to the nature of the data to which our analysis is aimed (photometry of low resolution spectra of unresolved sources), we have chosen to adopt the DUSTY code (Ivezić et al., 1999) to provide 1D radiative transfer modeling of stationary circumstellar envelopes in spherical symmetry. Although

DUSTY does offer the option to solve the hydrodynamic of self consistent radiative driven winds, we have chosen to disable this feature, in order to simplify the basic assumptions in our parameter grid.

As described in sections 2.1.5 and 2.1.6, a complete model of spherically symmetric AGB dusty envelopes is essentially described by the following parameters: (1) the total optical depth τ_V of the envelope, (2) the temperature T_1 of the inner boundary of the dust shell, (3) the shape of the spectral energy distribution of the central star and (4) the optical properties of the dust. In the following sections our choices for these modeling parameters are described. The models thus produced are then used in section 3.3 for the calibration of our mid-IR tools. In chapter 4 the same models are used to study correlations between AGB long period variability and the temporal modulation of their mass loss, and in chapter 5 to analyze our mid-IR images of selected AGB sources.

3.2.1 Opacities for AGB circumstellar dust

The chemical characterization of AGB circumstellar envelopes enters in the modeling procedure with the choice of a suitable opacity. According to the C/O abundance ratio, the chemistry of dust formation favors the condensation of either C-rich (around carbon stars) or O-rich dust (in low mass M-stars, or intermediate mass HBB AGBs). Separate opacities for the two cases are needed, in order to simulate the two classes of objects.

Since its discovery (Wolf & Ney, 1969), the 9.8 μm feature observed in the spectra of O-rich AGB stars was associated with the presence of silicate dust in the circumstellar environment. Early attempts to reproduce the energy distribution of the observed sources using the optical properties of laboratory grains failed, due to the inadequacy of crystalline terrestrial silicates (pyroxenes, olivines) to explain the high opacity of astronomical dust in the near-IR. The concept of *dirty silicates* was thus introduced by Jones & Merrill (1976), referring to an undetermined mixture of amorphous and crystalline materials, containing various types of impurities responsible for the required increase in opacity.

A widely used opacity for astronomical silicates was then derived by Volk & Kwok (1988), by manually adjusting the dust absorption coefficients used in their radiative transfer model, in order to reproduce the average spectra of O-rich envelopes with low optical depth and similar colors. From this opacity, Ossenkopf et al. (1992) computed two sets of optical constants, chemically and physically consistent according to the Kramers-Kronig relations and Mie theory (see sections 2.2.3 and 2.2.2). The two set of opacities

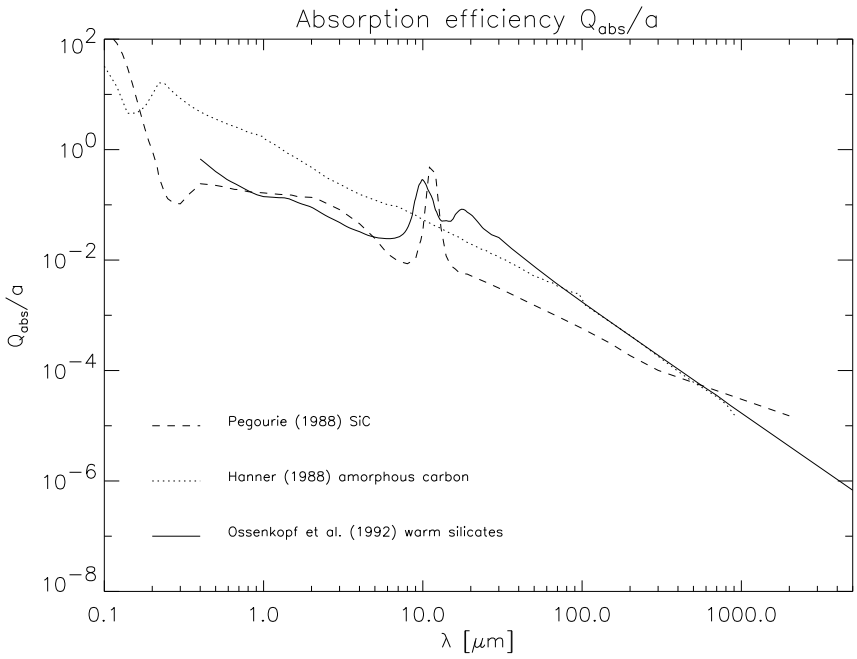

FIG. 3.5.— Dust opacities used in DUSTY modeling of our AGB envelopes. Amorphous carbon from Hanner (1988) (dotted line), SiC from Pégourié (1988) (dashed line), and "astronomical" silicates from Ossenkopf et al. (1992), warm set (solid line)

take into account the possibility of dust annealing in the circumstellar environment, as described by Stencel et al. (1990) and Nuth & Hecht (1990). The first set is optimized for "warm" silicates (expected to be found in sources with low optical depths, in which the oxidation of the silicate grains is not complete), and the second for the "cold" silicates (characteristics of very opaque envelopes, with "evolved" dust having higher content of Fe).

Since most of the sources in our test sample have low or intermediate optical depth, we have based our analysis on the adoption of the Ossenkopf et al. warm silicates opacity only, that are available in the standard DUSTY distribution.

A word of caution: is evident by the process in which such opacities have been produced, that they should be considered only as an "average" for the whole class of O-rich AGB circumstellar envelopes with low optical depth. By no means they can reproduce the exact shape of the 9.8 μm silicate feature for all sources, since a certain mineralogical variability should be expected between sources having different evolutionary status and metallicity.

In particular, Volk & Kwok arbitrarily set the ratio between the 10 and 18 μm features to be 0.5, while finding a possible range between 0.4 and 0.7, and this problem has only been partially fixed by Ossenkopf et al. increasing the ratio to the value of 0.55, which provides a better fit of laboratory data. A variation in this number, however, should still be expected, according to the relative abundance between Fe and Mg in the silicate structure. Furthermore, Ossenkopf et al. opacities cannot reproduce the observed 13 μm feature found in the IRAS spectra of many sources (tentatively associated to the presence of Al_2O_3 grains, see e.g. Onaka et al. 1989), or fit the crystalline silicate features observed in the ISO spectra of other envelopes. Even though suitable opacities for many amorphous and crystalline silicates and oxide materials are now available, and have been used to test the detailed chemical composition of individual envelopes (see e.g. Speck, 1998), such kind of analysis is outside the scope of this work. We are more interested in the determination of the thermal and density structure of AGB envelopes as a class, and thus our priority lies in fitting the whole LRS spectral region, and not in the details of the silicate feature alone. For this reason, the choice of the "warm" Ossenkopf et al. opacity appears to be adequate.

Concerning the opacity of dust in C-rich envelopes found around carbon stars, at least two main components are required, as many sources show the 11.2 μm SiC emission feature, along with a continuum associated to amorphous carbon. Even though SiC is present in nature in two main forms, the hexagonal-romboedric α-SiC, and β-SiC with cubic crystalline structure, only α-SiC produces a stable feature at 11.2 μm. For this reason we have chosen the opacity by Pégourié (1988) which was derived by applying Mie theory to α-SiC laboratory data. To simulate the continuum opacity due to amorphous carbon, we have adopted the optical constants measured by Hanner (1988), also implemented in the DUSTY code.

Since different AGB envelopes having the same infrared excess (e.g. similar total optical depth) does show SiC features with different intensity, it will be assumed that the relative abundance of SiC and amorphous carbon can be variable. In principle, the combined opacities of amorphous carbon and SiC should depend on the way the two species are mixed (SiC micrograin embedded in an amorphous carbon matrix, or coating of one material around a core of the other, etc...). In the absence of experimental data on this subject, we have chosen to produce the total opacity Q_{abs}^{tot} as the weighted average of the two single absorption coefficients:

$$Q_{abs}^{tot} = (1 - x)\, Q_{abs}^{amC} + x\, Q_{abs}^{SiC} \tag{3.5}$$

where x is the relative abundance (in number density) between the number density of SiC grains and the total. Our model grid for the C-rich envelopes is characterized by x from 0 (no SiC) to 0.14.

From equations 2.54 and 2.55 it is evident that the total opacity, at least in the range of sizes of AGB circumstellar grains, depends linearly on the radius a; the global optical properties of the dust in each envelope will thus depend on the adopted grain size distribution. For our grid of models, we have chosen to use the standard MRN distribution (see section 1.2.2), with grain size in the interval $0.005 \lesssim a \lesssim 0.25$ μm. This choice is justified by the greater uncertainty that are present the dust optical constants themselves, but should be regarded as a crude approximation of the real distribution, which may be enhanced toward larger grains in envelopes where grain growth is favored.

3.2.2 Model spectra for the central AGB star

At mid-IR wavelengths, where the dust thermal emission is maximum, the radiation of the central star contributes for only a small fraction of the total source spectra. For this reason, the spectrum of the AGB star powering the envelope can be in many cases approximated with a warm black body ($T_{eff} \sim$ 2000–3500 K). After running a number of test model grids with various T_{eff}, we concluded that the best results for the whole test sample of sources was obtained with $T_{eff} \sim 2000$ K; we have thus adopted this value for our full grid of models. One should take into account, however that in the mid-IR range the final spectra is not really sensitive to small variations in T_{eff}, and the chosen value is thus only representative of the observed spread in the effective temperature along the Asymptotic Giant Branch of the HR diagram.

A corollary of the scarce sensitivity of mid-IR to the stellar effective temperature, is the low precision in attempting to estimate the distance of AGB sources by fitting the mid-IR spectra. Due to the scaling properties of radiative transfer (see section 2.1.5), once the scaling factor Ψ is determined by fitting the source spectra, the spatial scale of the system is given by the ratio between T_1 and the T_{eff}:

$$\Psi = 4 \left(\frac{R_1}{R_*} \right)^2 \left(\frac{T_1}{T_{eff}} \right)^4 \tag{3.6}$$

Due to the poor determination of T_{eff} (and the fact that the ratio T_1/T_{eff} is elevated at the fourth power), also R_1 (and thus the bolometric

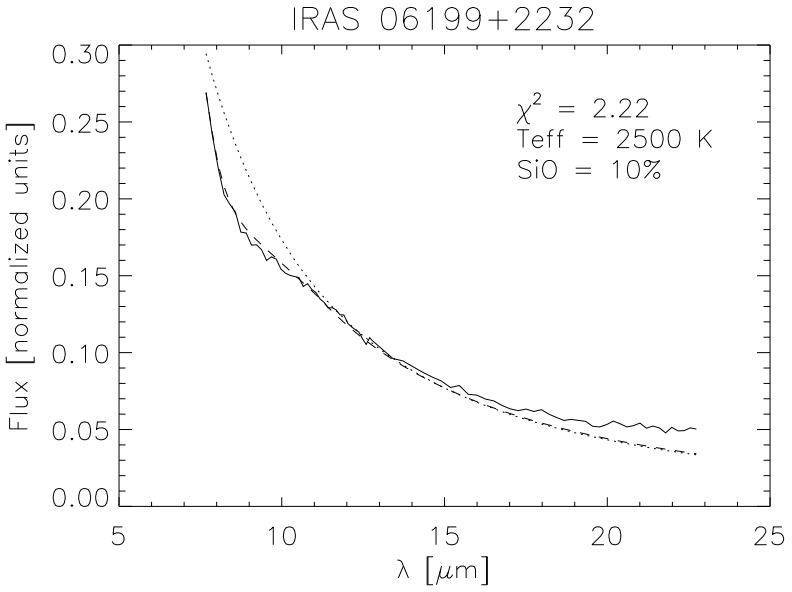

FIG. 3.6.— The spectrum of μ Gem (solid line) compared with an Engelke function of T_{eff} = 2500 K and SiO absorption of 10% (dashed line), and a black body with the same T_{eff} (dotted line). The source is a "naked photosphere" of spectral type M3III. Note the lower quality of the fit for $\lambda \gtrsim 15$ μm: an accurate model at larger wavelengths requires to add a dust cold shell with $\tau_V \simeq 10^{-3}$ and $T_1 \simeq 140$ K, showing that even this source (not an AGB) is surrounded by dust.

flux, see equation 2.25), cannot be well measured. A much better determination of the source distance requires a more precise fit of T_{eff}, that can be obtained only by detailed modeling of the stellar spectra, when the dust extinction is not excessive at optical and near infrared wavelengths.

For optically thin sources, a larger contribution from the central star should be expected. For these sources we have tested an alternative spectral distribution for the AGB star, that in principle should be more accurate in reproducing the continuum of late type giant stars. As described in Cohen et al. (1992), the main shortcoming of black bodies, when used to reproduce the spectrum of cool O-rich (M type) stars, is the presence of neutral hydrogen absorption and SiO line blending in the 8–10 μm range. This first feature can be effectively modeled using a wavelength dependent modification of the Planck black body, known as "Engelke function" (Engelke, 1992):

$$B_\nu^{(Engelke)}(T_{eff}) = B_\nu^{(Planck)}(T_b) \tag{3.7}$$

$$T_b = 0.738 \cdot T_{eff} \left(\frac{79450}{\lambda \cdot T_{eff}} \right)^{0.182} \tag{3.8}$$

where T_b is the color dependent *Engelke temperature*, which substitutes the effective temperature T_{eff} in the Planck function.

As a model for the SiO absorption, we have used the α Tau spectrum collected by Cohen et al. (1992). By subtracting an appropriate Engelke function with T_{eff} = 10,000 K from the α Tau spectrum, we extracted the features related to SiO absorption for that star. In order to produce a model of such absorption scalable for different amount of SiO, we have fitted the α Tau SiO feature with a 5th order polynomial. The generic AGB model spectra with given T_{eff} and SiO is then produced adding to the Engelke function the SiO fit polynomial, renormalized to produce the requested absorption at the nominal wavelength of 8 μm.

Even though this approximation is not a real SiO absorption spectrum, it can considerably improve the fitting of optically thin AGB sources and other "dustless" giants at IRAS LRS wavelengths, as shown in Sloan & Price (1995); an example is given in figure 3.6. This modified Engelke function with arbitrary T_{eff} and SiO absorption is part of the DUSTY distribution since version 2.0.

In the following discussion, to provide the best possible stellar photosphere without having too many free parameters, we have adopted, along with the "standard" black body with T_{eff} = 2500 K, an Engelke function with T_{eff} = 2500 K and SiO absorption of 10% as model photosphere for a second set of DUSTY simulations of O-rich envelopes.

3.2.3 Model parameter space

In order to reduce the number of models necessary to fit all the sources in our sample, we have restricted the free parameters in our DUSTY simulations to the optical depth τ_V, and the dust temperature T_1 at the inner envelope radius. This last quantity can either be seen as the dust condensation temperature for systems which are actively producing dust at present time, or the temperature at radius R_1 of the central cavity, which forms when the shell is detached due to a quiescent phase in the dust production. If the radius R_1, due to the scaling properties described in section 2.1.5, is completely determined by the choice of T_1, we set the outer radius R_2, which depends on the duration of the mass loss phase, to the fixed value of $1000 \cdot R_1$ for all models.

As described previously, we adopted the Ossenkopf et al. "warm" silicates as dust opacity of O-rich envelopes, and Hanner amorphous carbon mixed with a variable amount of Pégourié SiC for C-rich sources. The central AGB sources were modeled with both a 2000 K black body, and a 2500 K Engelke function with 10% SiO absorption (see previous section). All models were computed in spherical geometry, and the radial density distribution of the dust was assumed to be $n_d(r) \sim r^{-2}$ (steady mass loss for the period in which the dust shell was created). A set of models in which the radial structure was determined by full hydrodynamic dust driven stationary wind was also computed, by turning on this feature in DUSTY. This test showed only small differences between the spectra of "steady mass loss" and "radiatively driven winds" models; for this reason the discussion that follow will be made using the models with $n_d(r) \sim r^{-2}$.

As shown in Marengo et al. (1999), the modeling of O-rich sources of intermediate optical depth can be tricky, because the combination of low τ_V and high T_1 can produce silicate features very similar to the ones of models with higher opacity and low temperature shells. The two families of models, however, have different continuum slopes that can help in the discrimination. A fine grid of models is required to attempt the identification of a correct set of parameters on individual sources from their spectra. For this reason we run our models on a logarithmic grid with τ_V from 10^{-3} to 231, and T_1 from 100 to 1400 K for silicates, and 1000 K for carbonaceous dust (close to the respective dust condensation temperatures), with 60 steps in τ_V and 31 in T_1. A test with a finer grid of models didn't show any improvement in fitting individual sources, while a coarser grid did produce unreliable results.

3.3 Mid-IR colors of AGB dusty envelopes

The current size of available infrared telescopes, combined with the sensitivity of modern mid-IR imaging cameras, allow to spatially resolve only a minority of dusty circumstellar envelopes around AGB stars. The physical, chemical and evolutionary status of unrefolved sources can however be derived with the diagnostic tools here presented. This tools are calibrated with the help of our grid of radiative transfer models and the test sample of AGB sources. An application of these instruments is then given in chapter 4 to study the correlations between AGB long period variability and mass loss, and in chapter 5 to analyze the photometry of a sample of AGB envelopes imaged at various mid-IR telescopes.

3.3.1 A mid-IR photometric systems

The so-called "mid-IR window" is the spectral region between 7 and 13 μm in which the atmosphere is transparent enough to allow ground based astronomical observations. To make a use of this wavelength range, the first "thermal infrared" bolometers were using a broad band filter ($\Delta\lambda \sim 5$ μm) centered at the wavelength of 10 μm (N band filter). With the progresses in manufacturing more and more sensitive semiconductor arrays tuned to the infrared, the possibility of using filters with a smaller passband ($\Delta\lambda/\lambda \sim 0.1$, or 10% passband filters) allowed the development of a multiband photometric system in the mid-IR.

Modern mid-IR imaging cameras are equipped with a full set of 10% filters, designed to select specific features of thermal emission from dust and molecules emitting in the 10 μm region. In particular, two filters are used to image the continuum emissions at 8.5 and 12.5 μm, beginning and ending points of the mid-IR window. Another filter at 9.8 μm is designed to select the emissions at the center of the silicate feature, while a filter at 11.2 μm is centered with the SiC feature. More recently, with the further improvements in detectors sensitivity, filters at 18-20 μm have been introduced to take advantage of the relative resurgence of atmospheric transparency at these wavelengths.

Narrow band 2% filters are now available as part of "circular variable filters" (or CVF), able to perform low resolution imaging spectra of bright objects, and pin-point the wavelengths of specific features such as PAH emission lines. However, we use here the 10% passband filters at 8.5, 9.8, 11.2, 12.5 and 18 μm, since they are more specific to the emission of AGB dust, and are a "standard" set in all mid-IR infrared cameras.

The ability of a specific filter to transmit the radiation at the wavelength λ is described by the transmission function $\phi(\lambda)$. In the ideal case $\phi(\lambda)$ should be a top-hat function having maximum transparency in the passband $\Delta\lambda$, and zero outside. In practice, since the *profile* $\phi(\lambda)$ is determined by the manufacturing process, it can change between different filters, and have an irregular shape. To standardize our analysis without limiting the conclusions to a specific set of filters, we adopt for each filter a symmetric gaussian profile having FWHM equal to $\lambda/10$:

$$\phi_{\lambda_0}(\lambda) = N_0 \exp\left[-\frac{(\lambda-\lambda_0)^2}{\sigma^2_{\lambda_0}}\right] \tag{3.9}$$

where the normalization coefficient N_0 is defined to have $\int \phi(\lambda) = 1$, and

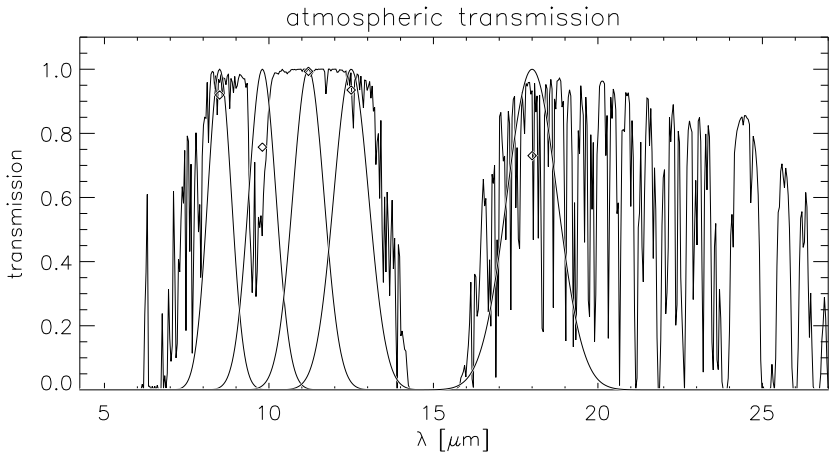

Atmospheric extinction coefficients

λ_{eff}:	8.50	9.80	11.20	12.50	18.00
trans:	0.920	0.757	0.994	0.935	0.730
τ_λ:	0.084	0.278	0.007	0.067	0.314
A_λ:	0.091	0.302	0.007	0.073	0.341

FIG. 3.7.— Atmospheric transparency in the mid-IR, measured at Mauna Kea, Hawaii (from United Kingdom Infra-Red Telescope (UKIRT) web site, program IRTRANS4). The gaussian profile of the filters in our mid-IR photometric system is superposed, and the average transparency in each filter passband is plotted (diamonds). In the lower panel the effective wavelength, average transparency, atmospheric optical depth and extinction of each filter is given.

$$\sigma_{\lambda_0} = \frac{\Delta\lambda_0}{2\sqrt{\log 2}} \tag{3.10}$$

These photometric bands can be combined to give a set of *colors* sensitive to the mid-IR dust features and continuum, defined as:

$$[\lambda_1] - [\lambda_2] = 2.5 \log \left[\frac{F_{\lambda_2}}{F_{\lambda_1}}\right] \tag{3.11}$$

The following colors are of interest in analyzing the emission of dusty circumstellar envelopes: the "blue continuum" color [8.5]-[12.5] sensitive to the slope of the dust thermal emission, the "red continuum" [12.5]-[18.0] measuring the infrared excess at longer wavelength, the "silicate" color [8.5]-[9.8] tuned to the 9.8 μm silicate feature and the "SiC" color [8.5]-[11.2] aimed to detect the presence of the SiC emission feature in C-rich envelopes.

We propose to show that this multiband photometric system is particularly suitable for exploring the characteristics of AGB circumstellar envelopes, and allows a simple immediate comparison with the predictions of sophisticated radiative transfer models.

3.3.2 A test sample of AGB sources

Since the aim of this analysis is to look into the correlations between AGB mass loss and mid-IR photometry, our working sample was extracted from a catalog of AGB stars with known mass loss rates, compiled by Loup et al. (1993) using millimetric observations of CO and HCN line observations.

The catalog (hereafter L93) consists of 444 sources, for which ^{12}CO(1→0), ^{12}CO(2→1) and HCN(1→0) circumstellar line observations have been published from 1995 through September 1992. This catalog is not complete, nor statistically significant, since it is clearly biased toward strong CO emitters. It is however a large sample, indicative of the general properties of AGB stars.

For each source in the L93 catalog, identified with an IRAS point source, the authors give an estimate of the total bolometric flux, based on the fit of the IRAS photometry at 12, 25 and 60 μm given in the IRAS Point Source Catalog (PSC, 1986). An estimate of the source distance is also available for 349 catalog objects, derived by assuming a "standard" luminosity of 10^4 $L_\odot$, and in some cases by modeling the CO and HCN emission.

For each source in the sample, L93 also gives an estimate of the total mass loss rate $\dot{M}$, by consistently determining the photodissociation radius R_{CO} (from which the CO emission is originated) with a numerical fit provided by Mamon et al. (1988). When detailed radiative transfer modeling of the CO line profile is made by the original authors of the observations more than one estimate is given. For all sources, the kinematic expansion velocity v_e of the CO/HCN shell is provided, inferred from the line profile.

In order to combine the mass loss information provided by the radio millimetric data with mid-IR photometry, we have extracted all the sources in L93 catalog for which a good quality IRAS LRS is available. With this additional criteria we ended up having a sublist of 154 O-rich, 7 S-type and 167 C-rich sources; note again that by construction this test sample suffers from the bias in the original L93 catalog, and also from the specific biases in the IRAS LRS, among which source confusion on the galactic plane.

The IRAS data were obtained for all sources from the Astrophysics Data Facility at NASA's Goddard Space Flight Center internet web server (`http://space.gsfc.nasa.gov/astro/iras`).

Table 3.1 IRAS color-color diagram regions

Region	Characteristic type of object
I	O-rich non variable stars without circumstellar shells
II	variable stars with "young" O-rich circumstellar shells
IIIa	variable stars with more evolved O-rich circumstellar shells
IIIb	variable stars with thick O-rich circumstellar shells
IV	variable stars with very thick O-rich circumstellar shells
V	planetary nebulæ and non variable stars with very cool circumstellar shells
VIa	non variable stars with relatively cold dust at large distances; a significant part of the stars is carbon rich
VIb	variable stars with relatively hot dust close to the star and relatively cold dust at large distances; some of the objects have proven to be O-rich
VII	variable stars with more evolved C-rich circumstellar shells
VIII	other objects

Each original spectrum was divided in two separate segments, corresponding to the *blue* and a *red* detectors of IRAS spectrometer (sensitive in the 8–13 and 11-22 μm wavelength range, respectively). We joined the two half of each LRS by superposing the overlapping region between 11 and 13 μm, as explained in the IRAS Explanatory Supplement (1988). The spectra were then rectified to correct for the wrong assumptions made on the spectrum of the LRS calibrating standard source (α Tau), as described in Cohen et al. (1992). The amount of this corrections is however generally small, and mainly affects the shorter wavelengths in the "blue" segment. The joint rectified spectra were then recalibrated to match the 12 μm IRAS PSC flux, by convolving the spectra with the IRAS 12 μm filter profile.

The IRAS LRS catalog provides an automatic classification two-digit code for each spectrum. The first digit (main class) is related to the spectral index β of the continuum (assuming $F_\lambda \propto \lambda^\beta$), while the second indicates the strength of the main feature, in emission or absorption, present in the mid-IR window. In particular, spectra of O-rich sources are identified by the strength of the 9.8 μm silicate feature, that is found in emission or absorption in the LRS classes 2n and 3n respectively. C-rich envelopes are

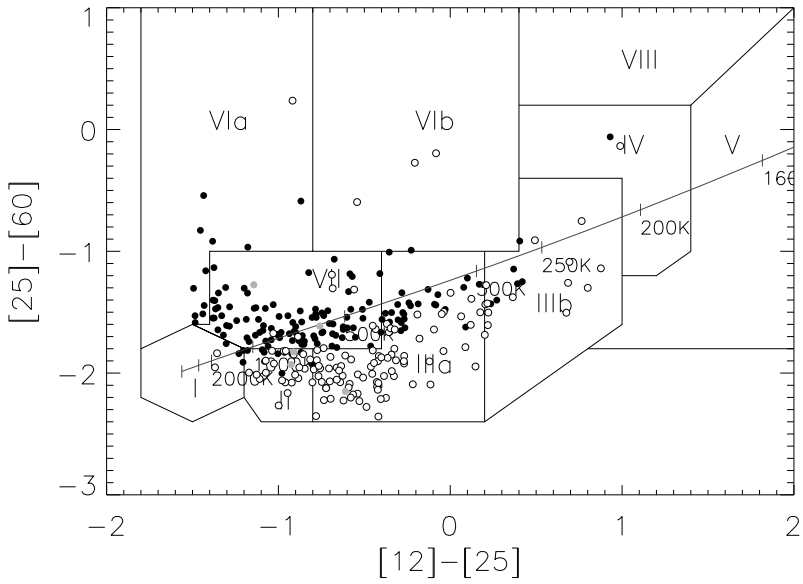

FIG. 3.8.— IRAS [25]-[60] vs. [12]-[25] color color diagram of test sources selected from Loup et al. (1993) catalog. Filled circles are C-rich sources, open symbols are O-rich and S-stars are plotted in gray. The regions in which the plot is divided are the ones defined by van der Veen & Habing (1988). The colors of black bodies at different temperatures are also indicated.

mainly found in the 4n class, defined by the strength of the 11.2 μm SiC feature in emission. Post-AGB objects of both types are in the main classes 6n and 7n, characterized by very large infrared excesses. Finally, both O-rich and C-rich sources may fall in classes 1n and 0n (featureless spectra), where a few LRS with self-absorbed SiC features can be found (Omont et al., 1993).

This classification is correlated to the infrared excess of the sources in the IRAS PSC photometry, as put in evidence by the IRAS [25]-[60] vs. [12]-[25] color-color diagram introduced by van der Veen & Habing (1988). Figure 3.8 shows the van der Veen & Habing color-color diagram of the test sample sources. The regions plotted on the diagram were identified according to the distribution of IRAS PSC sources on the diagram (see table 3.1).

The distribution of L93 sources is consistent with the van der Veen & Habing classification. Most of the O-rich sources are distributed in the

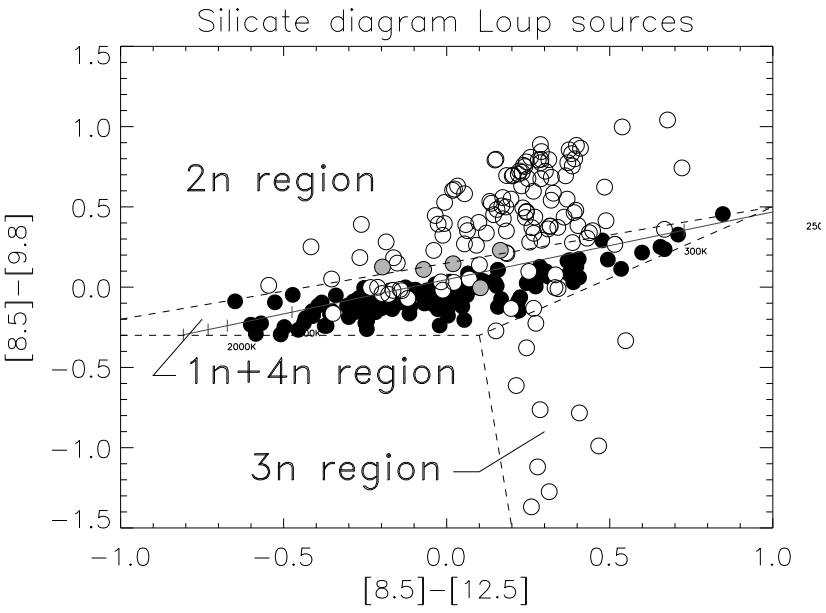

FIG. 3.9.— Silicate feature color color diagram of test sources selected from Loup et al. (1993) catalog. Filled circles are C-rich sources, open symbols are O-rich and S-stars are plotted in gray. The colors of black bodies with different temperatures are plotted, and the diagram is divided in three regions according to the LRS automatic classification of the sources.

II, IIIa and IIIb regions, in a sequence indicating a progressive increase in the source optical depth. Most of the C-rich sources are in region VII, as expected, even though some of them are located along the black body curve in region IIIa and IIIb. Only two sources are in region V, and are associated to post-AGB objects. The high 60 μm excess of the few sources in region VIa (mostly C-rich) and VIb (O-rich), may be due to the presence of a cold detached envelope, or to galactic cirrus contamination.

In order to simulate the mid-IR photometry for all the selected sources, we first converted the IRAS spectral energy distribution λF_λ in flux density units $F_\nu = \lambda^2 F_\lambda / c$, and then convolved F_ν with the gaussian filter profiles defined in section 3.3.1 for our photometric system:

$$F_{\lambda_0} = \int_0^\infty \phi_{\lambda_0}(\lambda) \cdot F_\nu(\lambda)\, \mathrm{d}\lambda \tag{3.12}$$

The derived photometry is then used to compute the mid-IR colors defined in section 3.3.1 for each source in the test sample.

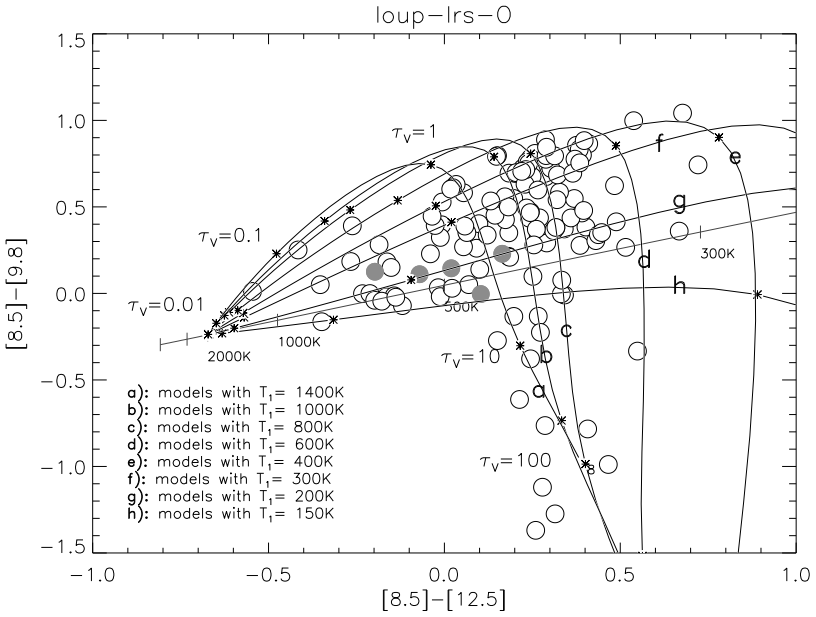

FIG. 3.10.— Silicate feature color color diagram of O-rich and S-stars with silicate dust DUSTY model tracks having T_1 of 1400, 1000, 600, 400 and 200 K; marks on each track indicate models having τ_V of 0.01, 0.1, 10 and 100.

3.3.3 The silicate feature color color diagram

A diagram sensitive to the strength of the 9.8 μm silicate feature is made by combining the [8.5]-[9.8] and the [8.5]-[12.5] colors. The distribution of our test sources is shown in figure 3.9. The diagram can be divided in three regions. The first is above the black body curve, and all the O-rich sources of LRS class 2n (with the silicate feature in emission) are found there. The second is aligned along the black body line, and groups all the C-rich sources plus the O-rich ones without the silicate feature (classes 4n and 1n respectively). Finally the third region is below the black body, and collects all the O-rich envelopes of class 3n (with the silicate feature in absorption).

The distribution of the C-rich sources on the diagram is apparently only a function of their increasing infrared excess, which causes a redder [8.5]-[12.5] color of thicker envelopes.

Concerning the O-rich sources, the explanation is apparently more complex, since a larger spread in both colors is present. This can be investigated by adding to the plot the colors of the silicate dust model envelopes

computed in section 3.2, derived from the model spectra by applying equation 3.12, similarly to what done for the sources. The result is shown in figure 3.10. Models with the "standard" black body of $T_s \simeq 2500$ K are used.

Each curve corresponds to a different temperature T_1, and is generated by models with increasing optical depth τ_V. Note that curves with a large ranges of T_1 are necessary to cover the whole area in which the sources are distributed. Envelopes located along the black body, having weak silicate feature and low color temperature, require T_1 as low as 200 K. Since dust cannot form efficiently at such low temperatures, this implies that a relatively large fraction of O-rich envelopes have shells which are detached from the dust forming stellar extended atmosphere, and have expanded to distances where the equilibrium temperature is consistently lower. In chapter 4 this hypothesis is tested on a sample of variable AGB stars, and correlated with the low period variability type (Mira, SR or Irregular).

It is important to note that model tracks for different T_1 join in the region of maximum source density. This means that the same silicate feature strength, relative to the continuum, can be obtained either with high T_1 and $\tau_V \gtrsim 1$ or with low T_1 and $\tau_V \lesssim 1$, and the two cases cannot be well separated on the basis of the mid-IR colors alone. To derive in a unique way the physical parameters of O-rich AGB circumstellar envelopes thus require considering the whole LRS distribution, or fitting colors in a larger wavelength range, in order to measure with higher sensitivity the slope of the continuum. The IRAS PSC fluxes can in principle provide the requested sensitivity, but in many cases produce spurious results due to galactic cirrus contamination at 60 and 100 μm.

Despite these limitations, the position of the model tracks on the diagram does explain the sources distribution. Sources above the black body have low and intermediate optical depths, as expected for LRS class 2n. Sources of class 1n appear instead as a combination between cold envelopes with low τ_V and hot shells with $\tau_V \sim 10$ (opacity at 10 μm close to unity), in which the silicate feature is partially self absorbed. Sources below the black body, on the other end, are below the black body line, due to their high τ_V which is responsible for the silicate feature in absorption.

3.3.4 The SiC color color diagram

The SiC color diagram, shown in figure 3.11 is very similar to the silicate color diagram. The O-rich sources, however do show a smaller spread, because the 11.2 micron filter still intercepts the last part of the 9.8 μm silicate

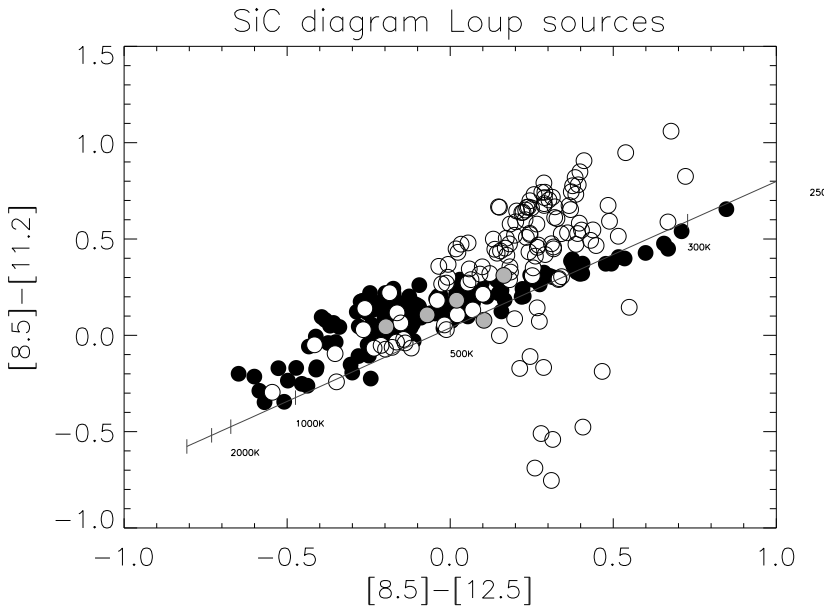

FIG. 3.11.— SiC feature color color diagram of all the sources in our test sample. Again filled circles are C-rich sources, grey symbols are S-stars and empty ones are O-rich. The black body line for different temperatures is also shown.

feature. The C-rich sources show instead a larger spread, and are located above the black body line; this is a direct consequence of the presence of the SiC emission feature in many sources.

This last statement is confirmed in figure 3.12, where carbonaceous dust radiative transfer model tracks are overplotted on the sources. Different lines are characterized by increasing amounts of SiC with respect to amorphous carbon, from 0 to 0.14 in number density of grains. Note that the displacements of the models for $\tau_V \sim 1$ is proportional to the abundance of SiC, as it increases the strength of the 11.2 μm feature. By fitting the two colors of the diagram, it should in principle be possible to estimate the SiC/amC ratio in the envelope of each source; the rather low S/N of most IRAS LRS, unfortunately, makes this task quite unpractical, and more accurate high resolution measurements of the 11 μm region are necessary. The plot, however, shows that for the L93 sample the maximum amount of SiC in the dust mixture is of the order of 14%, confirming that these grains are not a major component of C-rich dust.

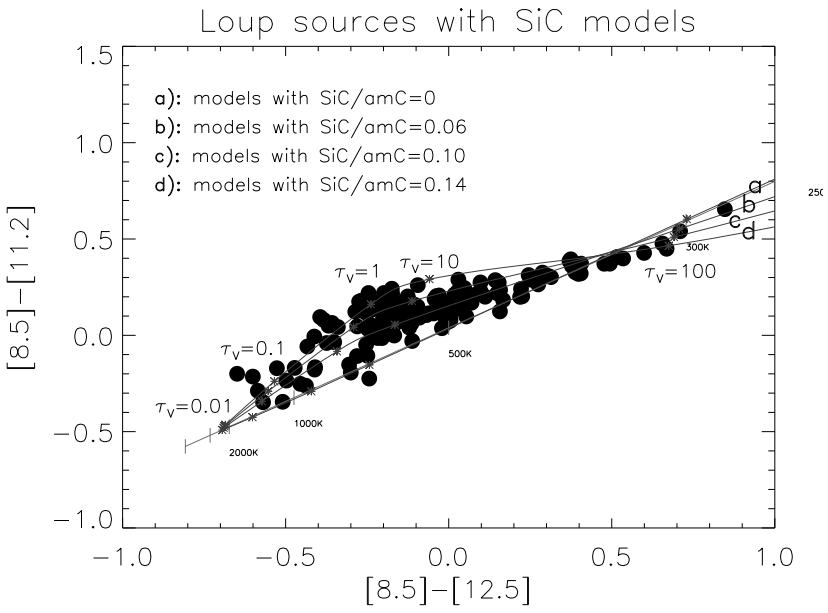

FIG. 3.12.— SiC feature color color diagram of C-rich sources with DUSTY model tracks having T_1 of 1000 K and SiC/amC abundance of 0, 0.06, 0.10 and 0.14. Marks on each track indicate models having τ_V of 0.01, 0.1, 10 and 100.

3.3.5 Mid-IR colors and mass loss rates

Equation 3.4 suggests that the mass loss rate of a dust-driven AGB wind should be proportional to the envelope optical depth τ_V and the stellar luminosity L_*, and inversely proportional to the outflow velocity v_e. Since the last two quantities, together with the total mass loss rate $\dot{M}$, are available for all sources in L93 catalog, we have defined a *mass loss parameter*

$$\mu = 2.5 \log \left[\left(10^5 \frac{\mathrm{d}M}{\mathrm{d}t} \right) \frac{v_e}{L_4} \right] \tag{3.13}$$

where L_4 is the luminosity in units of 10^4 $\mathrm{L}_\odot$. This quantity should be proportional to the optical depth τ_V.

As the infrared excess expressed by the [8.5]-[12.5] continuum color is related to τ_V (as demonstrated by the model tracks in figure 3.10 and 3.12) we tested this hypothesis with the diagram in figure 3.13.

The sources of different chemical type are not completely separated in the plot, but the C-rich sources appear to be more concentrated in the upper

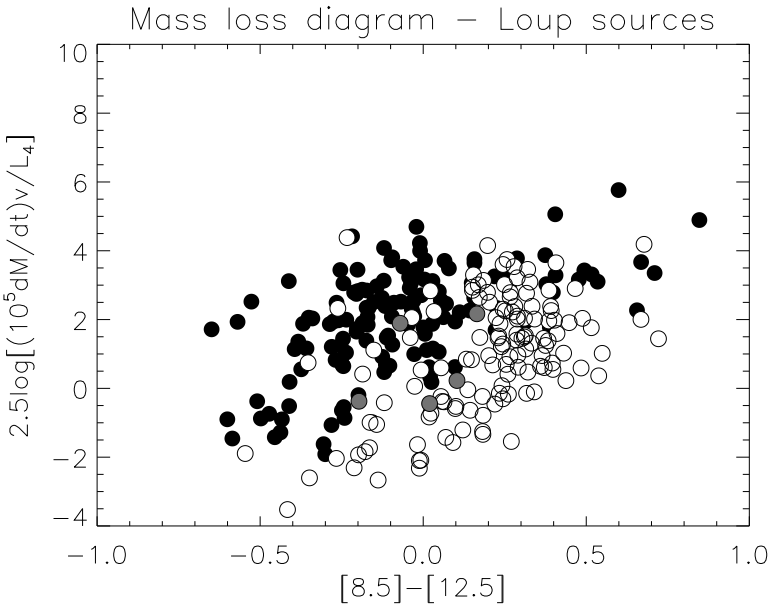

FIG. 3.13.— Mass loss rate parameter vs. infrared excess for L93 sources in test sample. C-rich envelopes are filled symbols, O-rich are empty and S-stars are grey circles.

left side of the diagram (higher mass loss, lower infrared excess), while the O-rich ones are grouped in the lower right side (redder colors and lower mass loss rates), with the few S-stars in between. The general increase of the mass loss parameter with the infrared excess, confirms that AGB mass loss is sustained by dust driven winds.

The partial segregation of the sources is explained by the different optical properties of the two dust opacities. Figure 3.5 shows that in the 10 μm window (and only in this region, due to the silicate features) the opacity of oxidic dust is higher than the absorption coefficient of carbonaceous material. As a result, the same quantity of dust in the circumstellar environment produces a larger infrared excess in O-rich sources than in C-rich envelopes.

Even though the error bars on the estimates of mass loss rate in the L93 sample are quite large, it is unlikely that the errors on $\dot{M}$ alone can explain the large spread in the source distribution shown in figure 3.13. This suggests that the spread is intrinsic for the sample, and possibly due to temporal variations in the mass loss rates on timescales smaller than the crossing time of the circumstellar envelope at the stellar wind speed. The L93 mass loss measurements are based on the CO emission taking place in a

shell of radius R_{CO}, of the order of 10^{17} cm, while the mid-IR photosphere is usually at a distance of about 10^{14}–10^{15} cm. To break the correlation between the gaseous and the dusty shells is required a temporal variation of $\dot{M}$ on timescales of the order of 10^3 yr (assuming an outflow velocity of 10 km s^{-1}), or shorter. This timescale is in general too short to be associated with the thermal pulses of the TP-AGB, and too long with respect to the long period variability ($P \sim 1$ yr) which characterize the AGB phase. They are however compatible with the temporal separation of structures observed in the remnant AGB shells of post-AGB objects like the Egg nebula (Sahai et al., 1998), or the evolved carbon star IRC+10216 (Mauron & Huggins, 1999) which have been associated to recurrent variations in the mass loss rate.